

# Interlayer Engineering Construction of 2D Nb<sub>2</sub>CT<sub>x</sub> with Enlarged Interlayer Spacing Towards High Capacity and Rate Capability for Lithium-Ion Storage

Mao-Cheng Liu,\*<sup>[a, b]</sup> Bin-Mei Zhang,<sup>[a, b]</sup> Yu-Shan Zhang,<sup>[a, b]</sup> Dong-Ting Zhang,<sup>[a, b]</sup> Chen-Yang Tian,<sup>[a, b]</sup> Ling-Bin Kong,<sup>[a, b]</sup> and Yu-Xia Hu\*<sup>[c]</sup>

The Li<sup>+</sup> storage rate capability and diffusion dynamics in two-dimensional (2D) materials are mainly determined by the interlayer spacing of materials. Investigating the effects of interlayer spacing on Li<sup>+</sup> diffusion rate in 2D materials can provide a theoretical guidance for developing the high rate 2D materials for Li<sup>+</sup> storage. Herein, a novel approach that P-phenylenediamine (PPDA) electrostatically intercalated into Nb<sub>2</sub>CT<sub>x</sub> layers is employed to facilitate fast Li<sup>+</sup> diffusion dynamics and improve diffusion rate for Li<sup>+</sup> storage. The PPDA molecules existed between Nb<sub>2</sub>CT<sub>x</sub> layers have “support and dragline” effects on layers structure during Li<sup>+</sup> insertion/extraction. The PPDA-Nb<sub>2</sub>CT<sub>x</sub> not only enlarges interlayer spacing ( $d=1.27$  nm) to accelerate the Li<sup>+</sup> diffusion rate, but also

enhances the layered structure stability due to the “support and dragline” effects of PPDA molecules. The PPDA-Nb<sub>2</sub>CT<sub>x</sub> exhibits the excellent capacity of 400 mAh g<sup>-1</sup> at a current density of 0.1 A g<sup>-1</sup> and displays a superior capacity retention as 70.2% at 5.0 A g<sup>-1</sup> compared with that of 0.5 A g<sup>-1</sup>. The PPDA-Nb<sub>2</sub>CT<sub>x</sub>//AC lithium ions hybrid capacitor (LIHC) delivers an excellent power density of 2754.8 W kg<sup>-1</sup> at an energy density of 58.3 Wh kg<sup>-1</sup> and a capacity retention with 80.0% at 1.0 A g<sup>-1</sup> after 1000 cycles. The interlayer engineering based on electrostatic intercalation provides a novel perspective to expand interlayer spacing, possessing a theoretical guidance for developing the Li<sup>+</sup> storage materials with high-rate capability.

## 1. Introduction

Two-dimensional (2D) materials have attracted the widespread attentions in energy storage fields due to their outstanding intrinsic properties, such as unique layered structure, large specific surface area, and high theoretical capacity.<sup>[1–6]</sup> The layered structure provides the high specific surface area and abundant ions diffusion channels compared with other bulk materials because of the unique layered structure, which is beneficial for fast ions diffusion between layers. The large specific surface area exposes more electrochemical active sites for ions storage,<sup>[7–8]</sup> while the weak Van der Waals forces between layers endow the possibility of interlayer engineering, which is crucial for improving the electrochemical storage

performance by expanding interlayer spacing.<sup>[9–14]</sup> Therefore, 2D materials have been viewed as the promising candidates for electrode materials with excellent ions storage performance and rate capability.

MXenes, a novel family of 2D materials, have attracted enthusiastic attentions, particularly in energy storage and conversion fields.<sup>[15–20]</sup> It is considered as an ideal electrode material of ions insertion type, in which the specific surface terminations (–O, –OH, and –F) of MXene can provide possibility for the interlayer modification.<sup>[21–22]</sup> Nb<sub>2</sub>CT<sub>x</sub>, a newly discovered and seldom reported MXene, exhibits a higher theoretical capacity than Ti<sub>3</sub>C<sub>2</sub> according to first-principles calculations.<sup>[23–24]</sup> For example, Naguib et al.<sup>[25]</sup> obtained Nb<sub>2</sub>CT<sub>x</sub> that demonstrates a reversible capacity of 170 mAh g<sup>-1</sup> at 1 C for LIBs. Mashtalar et al.<sup>[26]</sup> reported CNT/Nb<sub>2</sub>CT<sub>x</sub> composites exhibits a high specific capacity of 400 mAh g<sup>-1</sup> at 0.5 C for Li<sup>+</sup> storage. Liu et al.<sup>[27]</sup> developed N-doped Nb<sub>2</sub>CT<sub>x</sub> possesses the excellent Li<sup>+</sup> storage capacity (360 mAh g<sup>-1</sup> at 0.2 C) and superior cycling stability (288 mAh g<sup>-1</sup> at 0.5 C after 1500 cycles). The current research is mainly concentrated on improving the discharge capacity by doping or compounding other elements, while the issue that how to improve the Li<sup>+</sup> storage rate capability of Nb<sub>2</sub>CT<sub>x</sub> not be further discussed.<sup>[28–31]</sup> The related works of interlayer engineering modification indicates that expanding the interlayer spacing of Nb<sub>2</sub>CT<sub>x</sub> can provide abundant ions diffusion paths for Li<sup>+</sup> insertion/extraction for improving Li<sup>+</sup> diffusion dynamics. Such as the “pillar structure” effects are first proposed in multilayer Ti<sub>3</sub>C<sub>2</sub>T<sub>x</sub> MXene to explain the effects of large interlayer spacing on ions diffusion rate.<sup>[32]</sup> (i) Pre-intercalated cetyltrimethylammonium

[a] Dr. M.-C. Liu, B.-M. Zhang, Y.-S. Zhang, D.-T. Zhang, C.-Y. Tian, Prof. L.-B. Kong

School of Materials Science and Engineering  
Lanzhou University of Technology  
Lanzhou 730050, P. R. China  
E-mail: liumc@lut.edu.cn

[b] Dr. M.-C. Liu, B.-M. Zhang, Y.-S. Zhang, D.-T. Zhang, C.-Y. Tian, Prof. L.-B. Kong

State Key Laboratory of Advanced Processing and Recycling of Non-ferrous Metals  
Lanzhou University of Technology  
Lanzhou 730050, P. R. China

[c] Dr. Y.-X. Hu  
School of Bailie Engineering and Technology  
Lanzhou City University  
Lanzhou 730050, China  
E-mail: huyuxia@163.com

 Supporting information for this article is available on the WWW under  
<https://doi.org/10.1002/batt.202100083>

bromide (CTAB) is replaced with  $\text{Sn}^{4+}$  as a pillar and the interlayer spacing increase to 2.708 nm. (ii) The multilayer  $\text{Ti}_3\text{C}_2\text{T}_x$  MXene intercalated with different alkali metal cation exhibits the enlarged interlayer spacing and improved ions storage performance.<sup>[33]</sup> These results reveal that expanding interlayer spacing of  $\text{Ti}_3\text{C}_2\text{T}_x$  can effectively accelerate the ions diffusion dynamics and optimize the rate capability.<sup>[4,34–35]</sup> Therefore, enlarging the interlayer spacing of 2D materials is an effective strategy to improve  $\text{Li}^+$  diffusion dynamics and storage rate capability. However, as far as current works about exploring the relationship of interlayer spacing and rate capability of  $\text{Nb}_2\text{CT}_x$  not be reported. More importantly, revealing the relationships between interlayer spacing and ions storage rate capability are instructive for designing 2D materials with high-rate capability.

A facile and effective approach of electrostatic intercalation P-Phenylenediamine (PPDA) molecules between  $\text{Nb}_2\text{CT}_x$  layers has been demonstrated, which validly enlarges the interlayer spacing of  $\text{Nb}_2\text{CT}_x$  layers and delivers the fast  $\text{Li}^+$  diffusion dynamics and high diffusion coefficient. The PPDA- $\text{Nb}_2\text{CT}_x$  not only endows the large interlayer spacing to accelerate the  $\text{Li}^+$  diffusion, but also improves layered structure stability due to the “support and dragline” effects. The PPDA- $\text{Nb}_2\text{CT}_x$  exhibits the expanded interlayer spacing (1.27 nm) and high  $\text{Li}^+$  diffusion coefficient ( $1.5 \times 10^{-9} \sim 4.6 \times 10^{-7} \text{ cm}^2 \text{s}^{-1}$ ), which are

beneficial for  $\text{Li}^+$  diffusion between  $\text{Nb}_2\text{CT}_x$  layers. The PPDA- $\text{Nb}_2\text{C}$  displays an excellent specific capacity of 400  $\text{mAh g}^{-1}$  at a current density of 0.1  $\text{A g}^{-1}$  and the superior capacity retention of 70.2% at 5.0  $\text{A g}^{-1}$  compared with that of 0.5  $\text{A g}^{-1}$ . In addition, the PPDA- $\text{Nb}_2\text{CT}_x/\text{AC}$  LIHC delivers a high energy density of 100.3  $\text{Wh kg}^{-1}$  at a power density of 53.6  $\text{W kg}^{-1}$ . The method of electrostatic intercalation can enlarge the interlayer spacing and improve diffusion rate, which provides a theoretical guidance for developing  $\text{Li}^+$  storage materials with high-rate capability.

## 2. Results and Discussion

### 2.1. Structure and Morphology Characterization

The preparation schematic of PPDA- $\text{Nb}_2\text{CT}_x$  by electrostatically interaction is displayed in Figure 1a. The PPDA molecules are intercalated between  $\text{Nb}_2\text{CT}_x$  layers by electrostatic attraction, which effectively expands the interlayer spacing of  $\text{Nb}_2\text{CT}_x$  layers and achieves fast  $\text{Li}^+$  insertion/extraction. The PPDA molecules between  $\text{Nb}_2\text{C}$  layers have “support and dragline” effects to the layered structure, in which the “support” effects enlarge interlayer spacing to expose abundant accessible active sites for  $\text{Li}^+$  storage and the “dragline” effects relieve volume

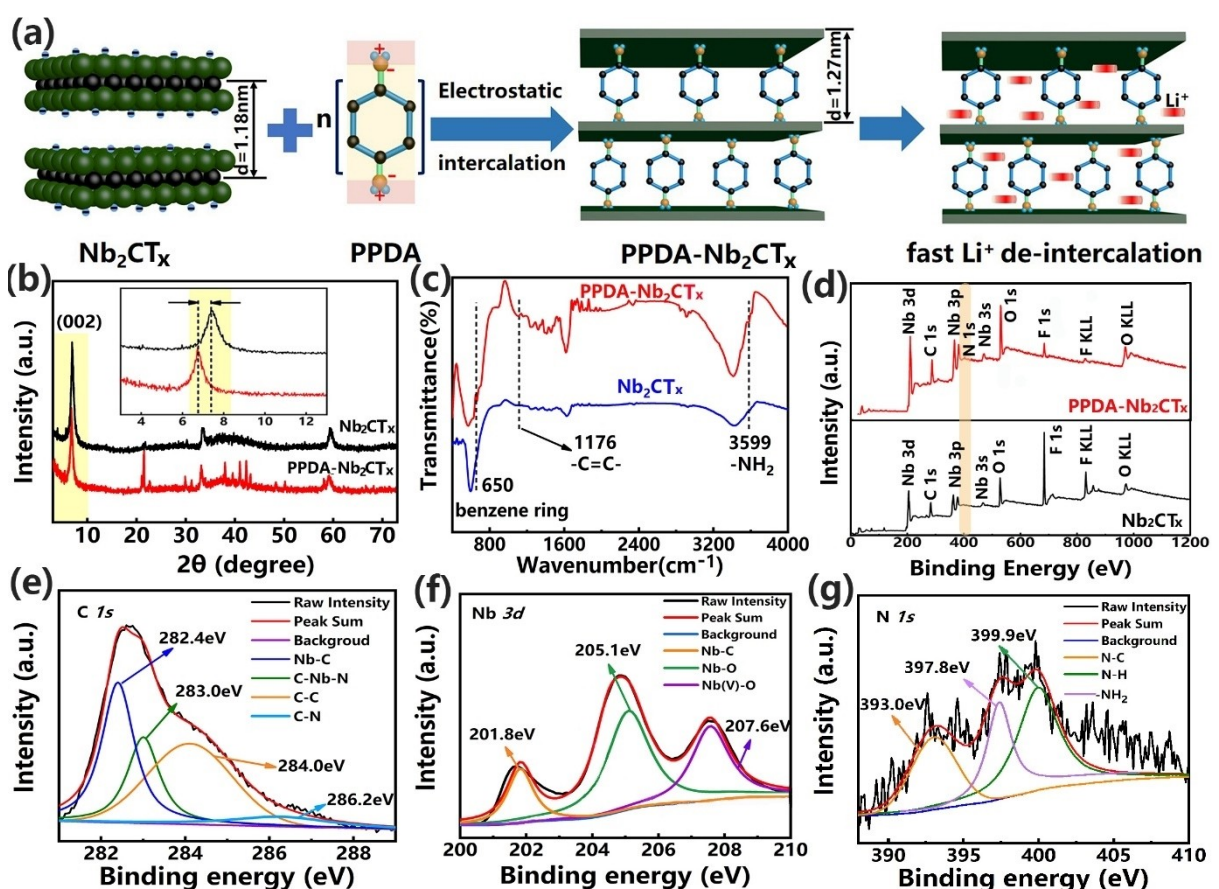


Figure 1. a) Schematic of the synthesis procedure for PPDA- $\text{Nb}_2\text{CT}_x$ ; b) XRD patterns; c) FTIR spectra; and d) XPS total-scan spectra of  $\text{Nb}_2\text{CT}_x$  and PPDA- $\text{Nb}_2\text{CT}_x$ . High-resolution XPS spectrum of PPDA- $\text{Nb}_2\text{CT}_x$ : e) C 1s; f) N 1s; and g) Nb 3d.

change to maintain the structure stability during  $\text{Li}^+$  insertion/extraction process. As shown in Figure 1b, the (002) diffraction peak of PPDA-Nb<sub>2</sub>CT<sub>x</sub> shifts to the left compared with that of Nb<sub>2</sub>CT<sub>x</sub>, revealing that the electrostatic intercalation of PPDA molecules can enlarge the interlayer spacing of Nb<sub>2</sub>CT<sub>x</sub> layers. The interlayer spacing of PPDA-Nb<sub>2</sub>CT<sub>x</sub> calculated from X-ray diffraction (XRD) pattern is 1.27 nm, which is beneficial for  $\text{Li}^+$  fast diffusion dynamics due to a low diffusion barrier. In Figure 1c, the Fourier transform infrared (FTIR) spectrum of PPDA-Nb<sub>2</sub>C appears three characteristic peaks at 3599 cm<sup>-1</sup>, 1176 cm<sup>-1</sup>, and 680 cm<sup>-1</sup>, which corresponds to -NH<sub>2</sub>, benzene ring functional group, and -C=C- bonds.<sup>[36–37]</sup> Those peaks indicate PPDA molecules successfully intercalate between Nb<sub>2</sub>CT<sub>x</sub> layers and form the chemical bonds. In addition, the FTIR spectrum of PPDA-Nb<sub>2</sub>CT<sub>x</sub> is nearly identical with that of Nb<sub>2</sub>CT<sub>x</sub>, which reveals that the chemical bonds of Nb<sub>2</sub>CT<sub>x</sub> are unchanged after electrostatic intercalation of PPDA molecules. The X-ray photoelectron spectroscopy (XPS) spectra are employed to further discuss the chemical state of PPDA-Nb<sub>2</sub>CT<sub>x</sub> as shown in Figure 1d. The new N 1s peak are originated from amino groups of PPDA molecules, which indicates PPDA-Nb<sub>2</sub>CT<sub>x</sub> are prepared successfully by the electrostatic interaction of Nb<sub>2</sub>CT<sub>x</sub> layers and PPDA molecules. The high-resolution C 1s spectrum of PPDA-Nb<sub>2</sub>CT<sub>x</sub> is displayed in Figure 1e, in where those peaks at 282.4 eV, 283.0 eV, 284.4 eV, and 286.2 eV are derived from the Nb-C, C-Nb-N, C-C, and C-N bonds, respectively. In Figure 1f, the strong peak at 201.8 eV is attributed to Nb-C bonds of PPDA-Nb<sub>2</sub>CT<sub>x</sub>. The other two peaks (Nb-O and Nb(V)-O) located at 205.1 eV and 207.6 eV are related to Nb<sub>2</sub>O<sub>5</sub>, which is attributed to the adsorption of oxygen elements on the surface. The spectrum of N 1s at 393.0 eV, 397.8 eV, and 399.9 eV corresponding to N-C, N-H, and -NH<sub>2</sub> bonds of PPDA-Nb<sub>2</sub>CT<sub>x</sub><sup>[38]</sup> (Figure 1g). Besides, the C 1s and Nb 3d spectra of Nb<sub>2</sub>CT<sub>x</sub> are similar with that of PPDA-Nb<sub>2</sub>CT<sub>x</sub> as shown in Figure S1, suggesting the intercalation of PPDA molecules has no effect on the chemical state of Nb<sub>2</sub>CT<sub>x</sub>. The N 1s spectrum proves PPDA molecules have tightly bonded with Nb<sub>2</sub>CT<sub>x</sub> layers through chemical bonds, which can not only enlarge the interlayer spacing of Nb<sub>2</sub>CT<sub>x</sub> owing to support effect, but also maintain structure stability due to dragline effect. The electrostatic interaction between Nb<sub>2</sub>CT<sub>x</sub> layer with PPDA molecules can provide straining effects to relieve the volume expansion during  $\text{Li}^+$  insertion and contribute pillaring effects to maintain the structure stability during  $\text{Li}^+$  extraction. The electrostatic interaction between Nb<sub>2</sub>CT<sub>x</sub> layer with PPDA molecules plays the important role for the excellent cycling stability and structure durability.

The typical accordion-like structure of Nb<sub>2</sub>CT<sub>x</sub> is clearly observed judging from the cross-section of scanning electron microscopy (SEM) images in Figure 2a. The adjacent layers are linked by the weak Van der Waals forces, which endows an opportunity for intercalating molecules between interlayers and tuning the interlayer spacing. The transmission electron microscopy (TEM) images of Nb<sub>2</sub>CT<sub>x</sub> exhibit the silk wrinkles which belongs to the typical layer-structure feature (Figure 2b). Moreover, the interlayer spacing corresponded to (002) plane of Nb<sub>2</sub>CT<sub>x</sub> is measured as 1.18 nm, which is consistent with the

result of XRD pattern (Figure 2c). The SEM and TEM images of PPDA-Nb<sub>2</sub>CT<sub>x</sub> are displayed in Figure 2d and 2e, the layered structure is still obvious after the intercalation of PPDA molecules, indicating the interlayer spacing of Nb<sub>2</sub>CT<sub>x</sub> layers is expanded while the layered structure is not destroyed. The corresponding high-resolution TEM images of PPDA-Nb<sub>2</sub>C as shown in Figure 2f, in which the interlayer spacing of 1.27 nm is larger than that of Nb<sub>2</sub>CT<sub>x</sub>. The PPDA molecules not only expand interlayer spacing of Nb<sub>2</sub>CT<sub>x</sub> but also weakens the ions diffusion barriers between interlayers, which is contributed to the fast  $\text{Li}^+$  diffusion dynamics. The element mappings of PPDA-Nb<sub>2</sub>CT<sub>x</sub> are shown in Figure 2g. The N elements originated from -NH<sub>2</sub> are uniformly distributed in Nb<sub>2</sub>CT<sub>x</sub> layers, suggesting that PPDA molecules are successfully intercalated between Nb<sub>2</sub>CT<sub>x</sub> layers by electrostatic interaction to form PPDA-Nb<sub>2</sub>CT<sub>x</sub> with the “support and dragline” layered structure. The PPDA-Nb<sub>2</sub>CT<sub>x</sub> with enlarged interlayer spacing not only offers the abundant transport pathways for  $\text{Li}^+$  diffusion, but also provides more accessible active sites for  $\text{Li}^+$  storage.<sup>[39–40]</sup>

## 2.2. Electrochemical performance

The half-cells of CR2032 coin-type were composed of working electrode (PPDA-Nb<sub>2</sub>CT<sub>x</sub>) and counter electrode (Li foil), and 1 M LiPF<sub>6</sub> (EC:DMC:EMC=1:1:1) was used as an electrolyte. The discharge capacity of PPDA-Nb<sub>2</sub>CT<sub>x</sub> with different ratio are tested as shown in Figure S2, in which 1.0 mg mL<sup>-1</sup> PPDA-Nb<sub>2</sub>CT<sub>x</sub> exhibits a higher specific capacity (400 mAh g<sup>-1</sup>) after 100 cycles than that of others. Therefore, the  $\text{Li}^+$  storage performance of 1.0 mg mL<sup>-1</sup> PPDA-Nb<sub>2</sub>CT<sub>x</sub> with the optimal sample is explored. The initial three cyclic voltammetry (CV) curves of PPDA-Nb<sub>2</sub>CT<sub>x</sub> between 0.01 V and 3.0 V potential with 0.1 mV s<sup>-1</sup> scan rate are presented in Figure 3a. The first CV curves of PPDA-Nb<sub>2</sub>CT<sub>x</sub> display one distinct oxidation peak and two reduction peaks, which is resulted from the irreversible reaction and initial solid electrolyte interphase (SEI) films.<sup>[41]</sup> Note that CV curves in the second and the third cycles are almost overlapped for PPDA-Nb<sub>2</sub>CT<sub>x</sub>, suggesting the excellent reversibility for  $\text{Li}^+$  storage. The three sharp peaks owing to the formation of SEI film during  $\text{Li}^+$  lithiation/delithiation process are also found for Nb<sub>2</sub>CT<sub>x</sub> in the first cycle (Figure S3a). Figure 3b exhibits the galvanostatic charge/discharge (GCD) curves of PPDA-Nb<sub>2</sub>CT<sub>x</sub> in the initial three cycles at the current density of 0.1 A g<sup>-1</sup>. The initial discharge capacity and charge capacity are 630.6 and 580.4 mAh g<sup>-1</sup>, revealing a superior initial coulombic efficiency (ICE) of 92.1%. Compared with Nb<sub>2</sub>CT<sub>x</sub> (Figure S3b to S3e), the excellent reversible capacity of PPDA-Nb<sub>2</sub>CT<sub>x</sub> is attributed to PPDA molecules electrostatically intercalated between Nb<sub>2</sub>CT<sub>x</sub> layers not only enlarges the interlayer spacing to expose more active sites for  $\text{Li}^+$  storage, but also offers abundant ions diffusion pathways to facilitate  $\text{Li}^+$  diffusion dynamics. The rate capability of PPDA-Nb<sub>2</sub>CT<sub>x</sub> is further investigated at different current densities as shown in Figure 3c and 3d, in which the discharge capacities are obtained as 380, 250, 170, 130, 100, and 80 mAh g<sup>-1</sup> at the current densities of 0.1, 0.2, 0.5, 1.0, 2.0, and 5.0 A g<sup>-1</sup>,

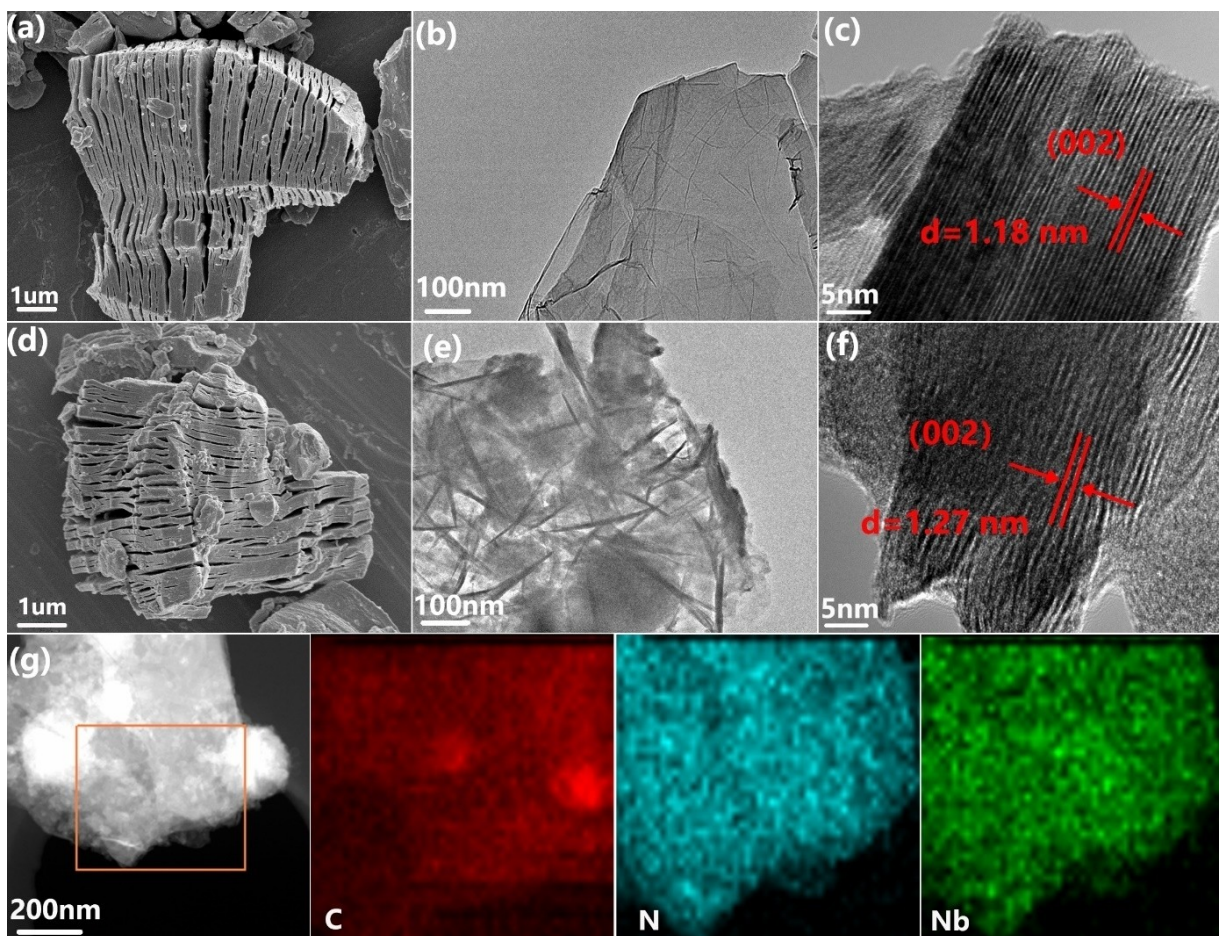


Figure 2. The SEM, TEM, and HR-TEM images of  $\text{Nb}_2\text{CT}_x$  are (a-c) and PPDA- $\text{Nb}_2\text{CT}_x$  are (d-f). g) Element mapping images of PPDA- $\text{Nb}_2\text{C}$ .

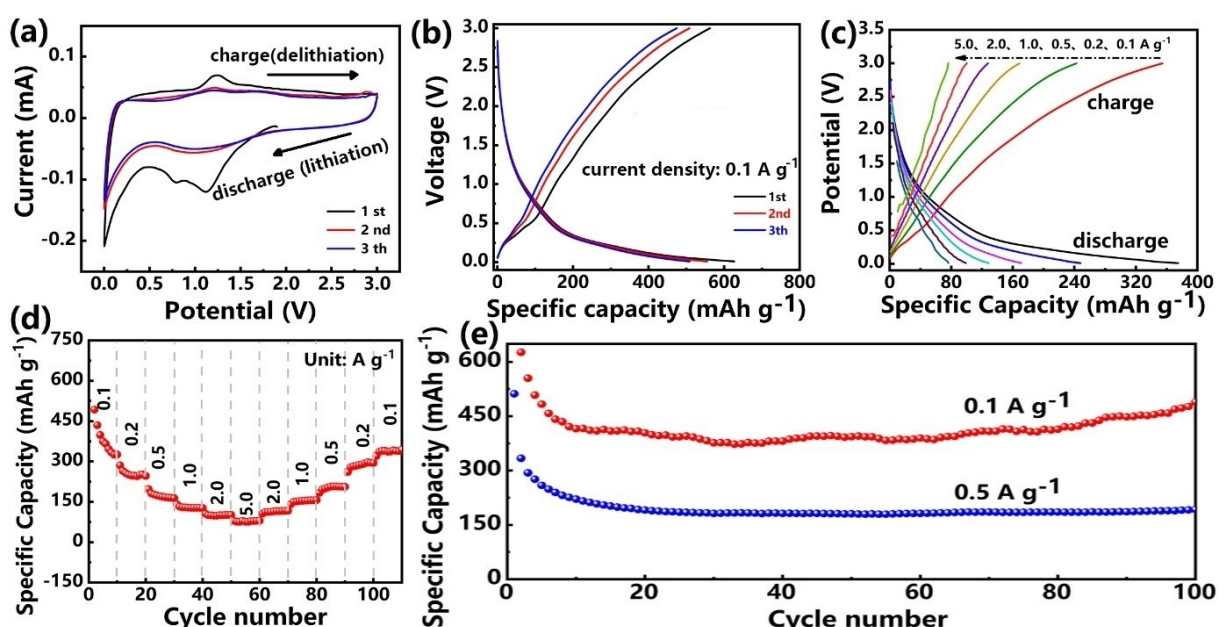


Figure 3. Electrochemical performance of PPDA- $\text{Nb}_2\text{CT}_x$ . a) The initial three CV curves at a scan rate  $0.1 \text{ mV s}^{-1}$ . b) The GCD curves at a current density of  $0.1 \text{ A g}^{-1}$ . c) The GCD curves at different current densities. d) Rate capability. e) Cycling performance at current density of  $0.1 \text{ A g}^{-1}$  and  $0.5 \text{ A g}^{-1}$ .

respectively. Moreover, the specific capacity of  $350 \text{ mAh g}^{-1}$  is retained when the current density recovers from  $5 \text{ Ag}^{-1}$  to  $0.1 \text{ Ag}^{-1}$ , which is explained that the PPDA molecules enlarge interlayer spacings and enhance the layered structure stability due to "support and dragline" effects. The PPDA-Nb<sub>2</sub>CT<sub>x</sub> exhibits the excellent Li<sup>+</sup> storage capacity and cycling stability due to the intercalation of PPDA molecules expands interlayer spacing and provides abundant active sites, in where a high reversible capacity of  $450 \text{ mAh g}^{-1}$  at  $0.1 \text{ Ag}^{-1}$  and  $198 \text{ mAh g}^{-1}$  at  $0.5 \text{ Ag}^{-1}$  are displayed in Figure 3e. The superior cycling stability is attributed to PPDA molecules between interlayers relieve volume change during Li<sup>+</sup> insertion/extraction process and maintain the structure stability due to "support and dragline" effects. Interestingly, the specific capacity of PPDA-Nb<sub>2</sub>CT<sub>x</sub> is gradually improving with the increase of cycle times in long-term cycling process. The main reason is the Li<sup>+</sup> diffusion channels of PPDA-Nb<sub>2</sub>CT<sub>x</sub> are gradually opened during the Li<sup>+</sup> insertion/extraction process, which improves the electrochemical utilization ratio of active materials and ameliorates the ions diffusion dynamics.

To further explore the effects of the interlayer spacing on Li<sup>+</sup> storage mechanism, the CV curves of PPDA-Nb<sub>2</sub>CT<sub>x</sub> and Nb<sub>2</sub>CT<sub>x</sub> at various scan rates from  $0.2$  to  $1.0 \text{ mV s}^{-1}$  are tested. In general, CV curves reflect the total current response which combines diffusion-controlled process and surface-controlled

process at the specific potential, providing a perspicuous perspective to understand the Li<sup>+</sup> storage mechanism (according to the Equations S1 and S2 in supporting information). The CV curves of PPDA-Nb<sub>2</sub>CT<sub>x</sub> at different scan rates as shown in Figure 4a, the rectangular-like shape of CV curves indicates PPDA-Nb<sub>2</sub>CT<sub>x</sub> possesses the hybrid energy storage mechanism. The shape of CV curves is maintained with the increasement of the scan rate, indicating the highly electrochemical reversibility of Li<sup>+</sup> storage in PPDA-Nb<sub>2</sub>CT<sub>x</sub>. However, the positions of reduction peaks shift to the low potential while oxidation peaks shift to the high potential with the increase of scan rate in CV curves, which attributes to the Li<sup>+</sup> diffusion rate can hardly satisfy the balance between charge transfer with phase consumption, resulting the reaction on surface is increased and the internal reaction is delayed.<sup>[42]</sup> The *b*-values of anodic and cathodic peaks are  $0.85$  and  $0.93$ , illustrating the surface-controlled capacitive reaction is dominant in electrode reaction of PPDA-Nb<sub>2</sub>CT<sub>x</sub>. The capacitive contributions of two behaviors are calculated by Equation S3, the surface-controlled capacitive contribution is  $78.0\%$  at a scan rate of  $0.2 \text{ mV s}^{-1}$  (Figure 4c). Notably, the surface-controlled capacitive contributions of PPDA-Nb<sub>2</sub>CT<sub>x</sub> at different scan rates are  $78\%$ ,  $84\%$ ,  $89\%$ ,  $93\%$ , and  $95\%$  as shown in Figure 4d. The surface-controlled capacitive contribution is gradually expanding with the increase of scan rate, suggesting the electrode reaction mainly

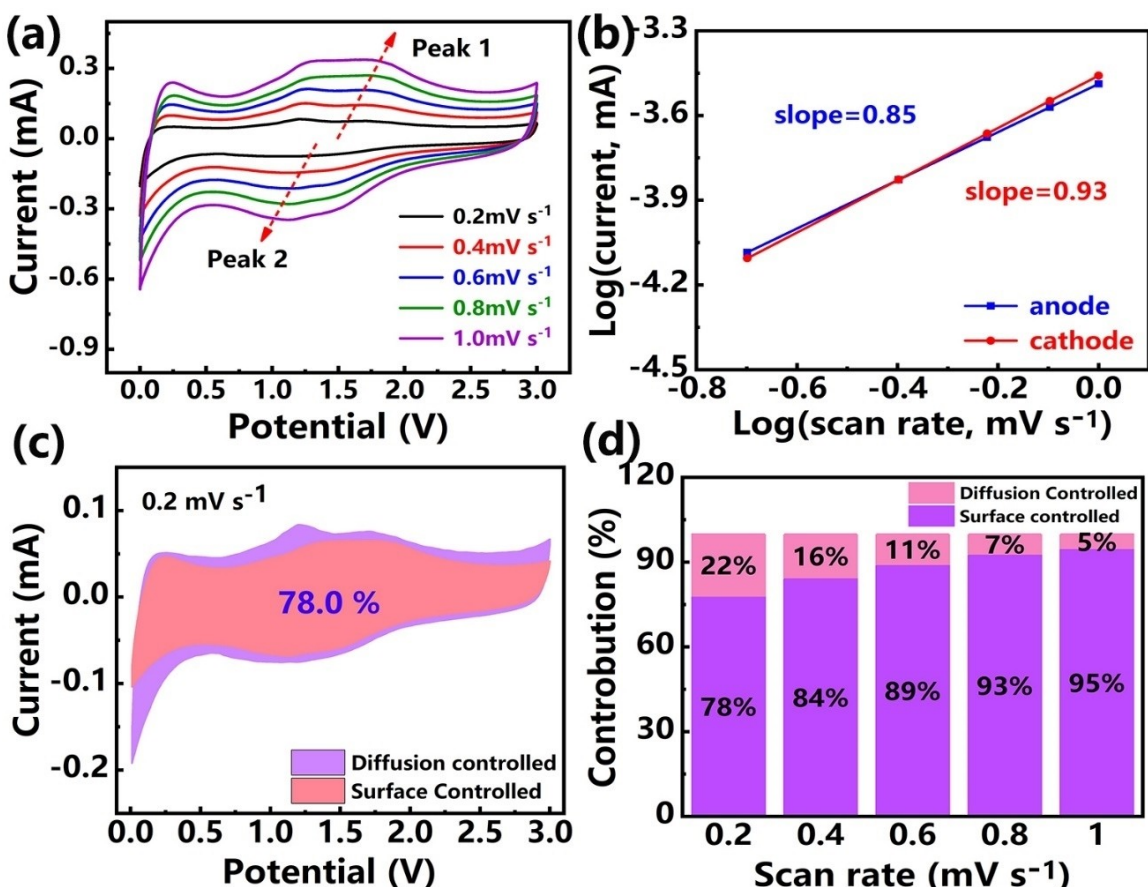
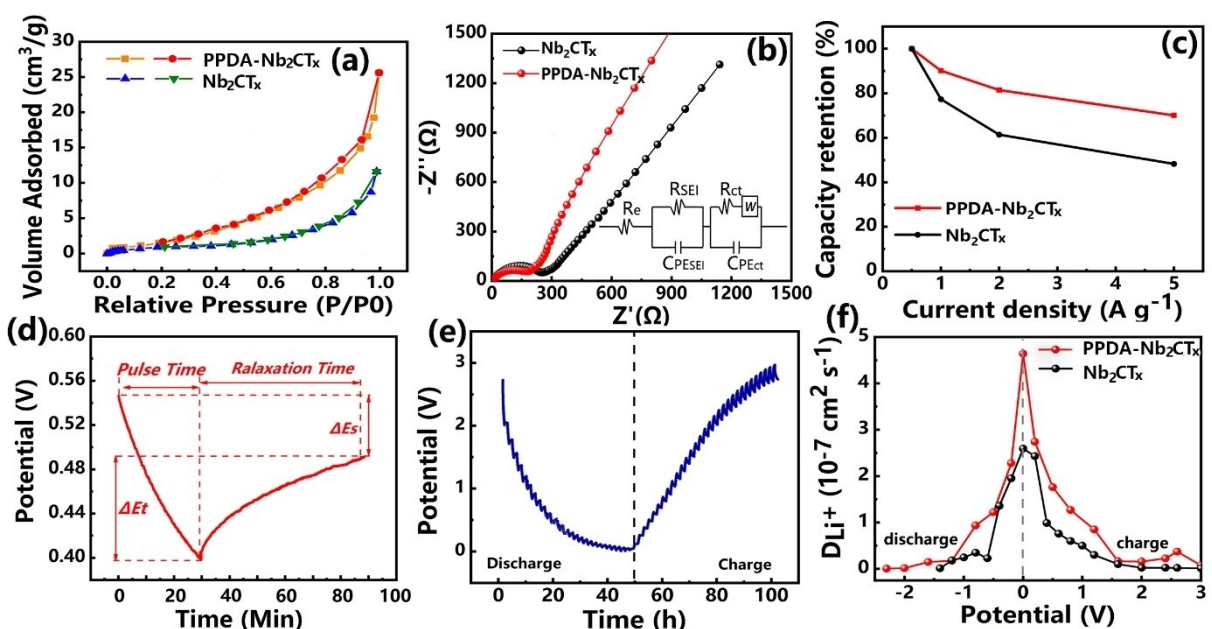


Figure 4. The Li<sup>+</sup> storage behavior of PPDA-Nb<sub>2</sub>CT<sub>x</sub>. a) CV curves at various scan rates from  $0.2$  to  $1.0 \text{ mV s}^{-1}$ . b) The *b*-value at peak currents. c) Contributions of two capacitive behaviors at  $0.2 \text{ mV s}^{-1}$ . d) Capacitive contributions of the surface-controlled and diffusion-controlled behavior at versus scan rates.



**Figure 5.** The dynamics analysis of PPDA-Nb<sub>2</sub>CT<sub>x</sub>. a) The N<sub>2</sub> adsorption/desorption isotherms. b) Nyquist plots before cycling. c) Capacity retention at different current densities. d) The single titration with GITT. e) The potential curves of GITT test. f) Li<sup>+</sup> diffusion coefficients.

occurs on surface of PPDA-Nb<sub>2</sub>CT<sub>x</sub> at high scan rate. According to Figure S4, the Li<sup>+</sup> storage mechanism of PPDA-Nb<sub>2</sub>CT<sub>x</sub> is similar with Nb<sub>2</sub>CT<sub>x</sub>. The surface-controlled capacitive contribution of PPDA-Nb<sub>2</sub>CT<sub>x</sub> is improved, revealing the PPDA-Nb<sub>2</sub>CT<sub>x</sub> with enlarged interlayer spacing can expose more available specific surface area to enhance the surface-controlled capacitive contribution for optimizing the rate capability.

### 2.3. Electrochemical Dynamics Analysis

The Li<sup>+</sup> diffusion dynamics of 2D materials is determined by its interlayer spacing within a certain extent. To clearly understand the relationship between the interlayer spacing of 2D materials and Li<sup>+</sup> diffusion dynamics, the effects of interlayer spacing on Li<sup>+</sup> diffusion coefficient and capacity retention are investigated. As shown in Figure 5a, the PPDA-Nb<sub>2</sub>CT<sub>x</sub> possesses a higher specific surface area ( $29.83 \text{ m}^2 \text{ g}^{-1}$ ) than Nb<sub>2</sub>CT<sub>x</sub> ( $8.86 \text{ m}^2 \text{ g}^{-1}$ ) due to the PPDA molecules between Nb<sub>2</sub>CT<sub>x</sub> layers enlarge the interlayer spacing. The Nyquist plot includes the charge transfer impedance in high frequency and diffusion impedance in low frequency, in where the semicircular portion represents charge transport impedance in materials and the straight portion means ions diffusion impedance. The fitting equivalent circuit consists  $R_e$  (the intrinsic impedance of electrode material),  $R_{SEI}$  and  $C_{peSEI}$  (the Li<sup>+</sup> diffusion impedance in SEI films),  $R_{ct}$  and  $C_{peCT}$  (the charge transfer impedance),  $C_{pe}$  (the constant phase element), and  $W$  (the Warburg impedance).<sup>[43]</sup> The electrochemical impedance spectroscopy (EIS) curves of before cycling as shown in Figure 5b, PPDA-Nb<sub>2</sub>CT<sub>x</sub> delivers a low  $R_e$  and  $R_{ct}$  from Table 1, confirming the increased interlayer spacing is prone to Li<sup>+</sup> diffusion for achieving fast ions storage dynamics. Figure 5c demonstrates the relationship between the current

**Table 1.** Fitting results of Nyquist plots.

Sample	Nb <sub>2</sub> CT <sub>x</sub>	PPDA-Nb <sub>2</sub> CT <sub>x</sub>
$R_e [\Omega]$	4.54	3.94
$R_{ct} [\Omega]$	171.9	89.6

density and capacity retention, in where PPDA-Nb<sub>2</sub>CT<sub>x</sub> demonstrates the capacity retention of 100%, 90.2%, 81.5%, and 70.2% at different current densities of 0.5, 1.0, 2.0, and  $5.0 \text{ A g}^{-1}$ , respectively. The obviously improved capacity retention of PPDA-Nb<sub>2</sub>CT<sub>x</sub> (the capacity retention of Nb<sub>2</sub>CT<sub>x</sub> is 48.3% at  $5.0 \text{ A g}^{-1}$ ) suggests PPDA-Nb<sub>2</sub>CT<sub>x</sub> possesses the superior capacity retention due to the “support and dragline” effects of PPDA molecules. As shown in Figure 5d, the galvanostatic intermittent titration technique (GITT) measurement can further disclose the Li<sup>+</sup> diffusion dynamics of PPDA-Nb<sub>2</sub>CT<sub>x</sub> and Nb<sub>2</sub>CT<sub>x</sub>. The GITT test consists of a series of “pulse + constant current + relaxation”. In addition, the Li<sup>+</sup> diffusion resistance of PPDA-Nb<sub>2</sub>CT<sub>x</sub> and Nb<sub>2</sub>CT<sub>x</sub> can be quantificationally evaluated by Li<sup>+</sup> diffusion coefficients, which is achieved from GITT measurements (Figure 5e and S5). According to Equation S4, the Li<sup>+</sup> diffusion coefficients of PPDA-Nb<sub>2</sub>CT<sub>x</sub> and Nb<sub>2</sub>CT<sub>x</sub> at different potentials can be obtained (the positive sign only represents charge process and negative sign represents discharge process).<sup>[44]</sup> In Figure 5f, the Li<sup>+</sup> diffusion coefficient ( $1.5 \times 10^{-9} \sim 4.6 \times 10^{-7} \text{ cm}^2 \text{ s}^{-1}$ ) of PPDA-Nb<sub>2</sub>CT<sub>x</sub> is higher than that of Nb<sub>2</sub>CT<sub>x</sub> ( $1.2 \times 10^{-9} \sim 2.6 \times 10^{-7} \text{ cm}^2 \text{ s}^{-1}$ ), indicating the intercalation of PPDA molecules can not only offer a large specific surface area to improve Li<sup>+</sup> storage performance, but also expand interlayer spacing to accelerate Li<sup>+</sup> diffusion rate. The results demonstrate that Li<sup>+</sup> diffusion dynamics and the rate capability are closely related to the interlayer spacing of 2D materials, expanding the interlayer spacing of 2D layered

materials can effectively improve  $\text{Li}^+$  diffusion dynamics and storage rate capability.

#### 2.4. Electrochemical Behavior of Lithium-ions Capacitor

The enlarged interlayer spacing provides abundant electrochemical active sites and diffusion channel for  $\text{Li}^+$  storage and rapid diffusion during insertion/extraction process. To further clarify the superior electrochemical storage performance of PPDA-Nb<sub>2</sub>CT<sub>x</sub>, the PPDA-Nb<sub>2</sub>CT<sub>x</sub>//AC lithium ions hybrid capacitor (LIHC) is constructed by employed PPDA-Nb<sub>2</sub>CT<sub>x</sub> as anode and active carbon (AC) as cathode in 1 M LiPF<sub>6</sub> electrolyte. The  $\text{Li}^+$  inserts/extracts into PPDA-Nb<sub>2</sub>CT<sub>x</sub> anode to achieve the charge storage during discharge/charge process, whereas PF<sub>6</sub><sup>-</sup> reversibly adsorbs/desorbs on the surface of AC cathode (Figure 6a). The quasi-rectangular shape of CV curves is maintained with the increase of scan rate in Figure 6b, suggesting the battery-type and electrical double-layer energy storage mechanism are coexistence and the electrode reaction is highly reversible. As displayed in Figure 6c, the GCD curves of PPDA-Nb<sub>2</sub>CT<sub>x</sub>//AC LIHC at various current densities are observed as the non-standard triangle shape, indicating the energy storage mechanism of capacitor-type is primary. The specific capacitance of PPDA-Nb<sub>2</sub>CT<sub>x</sub>//AC LIHC reaches 46.2 F g<sup>-1</sup> at the current density 0.1 A g<sup>-1</sup>, while the specific capacitance decreases from 41.7, 38.3, 35.4, 32.2 to 26.1 F g<sup>-1</sup> when the current density increases from 0.2 to 0.5 A g<sup>-1</sup> (Figure 6d). The capacitance retention of PPDA-Nb<sub>2</sub>CT<sub>x</sub> as 80% could be retained at current density of 1.0 A g<sup>-1</sup> after 1000 cycles, confirming that PPDA-Nb<sub>2</sub>CT<sub>x</sub>//AC LIHC possesses an excellent cycling stability with a high coulombic efficiency of 99.99%. Energy density and power density are important

factors for evaluating the electrochemical performance of LIHCs devices. Figure 6e exhibit the Ragone plots of PPDA-Nb<sub>2</sub>CT<sub>x</sub>//AC LIHC, which delivers a high energy density of 100.3 Wh kg<sup>-1</sup> at a power density of 53.6 W kg<sup>-1</sup> and it still maintains an energy density of 58.3 Wh kg<sup>-1</sup> at 2754.8 W kg<sup>-1</sup>. The energy storage performance of PPDA-Nb<sub>2</sub>CT<sub>x</sub>//AC is superior to that previously reported TiO<sub>2</sub>-rGO//AC,<sup>[45]</sup> Nb<sub>2</sub>O<sub>5</sub>-C//AC,<sup>[46]</sup> V<sub>2</sub>O<sub>5</sub>-rGO//AC,<sup>[47]</sup> SnO<sub>2</sub>-rGO//AC,<sup>[48]</sup> WO<sub>3</sub>-RGO//AC,<sup>[49]</sup> and MnO<sub>2</sub>-CNT//AC.<sup>[50]</sup> The excellent electrochemical performance indicates the approach of electrostatic intercalation is an effective strategy to enlarge interlayer spacing of 2D materials, which is beneficial for the high  $\text{Li}^+$  diffusion dynamics and the superior storage performance.

### 3. Conclusions

A novel approach of electrostatic intercalation PPDA molecules between Nb<sub>2</sub>CT<sub>x</sub> layers is proposed, which can effectively enlarge the interlayer spacing of Nb<sub>2</sub>CT<sub>x</sub> and facilitate fast  $\text{Li}^+$  insertion/extraction for achieving the excellent  $\text{Li}^+$  storage performance and fast diffusion dynamics. The PPDA-Nb<sub>2</sub>CT<sub>x</sub> not only endows large interlayer spacing to expose more active sites for  $\text{Li}^+$  storage, but also improves the stability of layered structure due to the "support and dragline" effects. The effects of interlayer spacing on  $\text{Li}^+$  diffusion dynamics are clarified, in which PPDA-Nb<sub>2</sub>CT<sub>x</sub> delivers the suitable interlayer spacing of 1.27 nm and the high diffusion coefficient ( $1.5 \times 10^{-9} \sim 4.6 \times 10^{-7} \text{ cm}^2 \text{s}^{-1}$ ) for fast  $\text{Li}^+$  de-intercalation. As a result, the PPDA-Nb<sub>2</sub>CT<sub>x</sub> exhibits an excellent capacity of 400 mAh g<sup>-1</sup> at a current density of 0.1 A g<sup>-1</sup> and displays a superior capacity retention as 70.2% at 5.0 A g<sup>-1</sup> compared with that of 0.5 A g<sup>-1</sup>. In addition, the PPDA-Nb<sub>2</sub>CT<sub>x</sub>//AC LIHC delivers a high energy

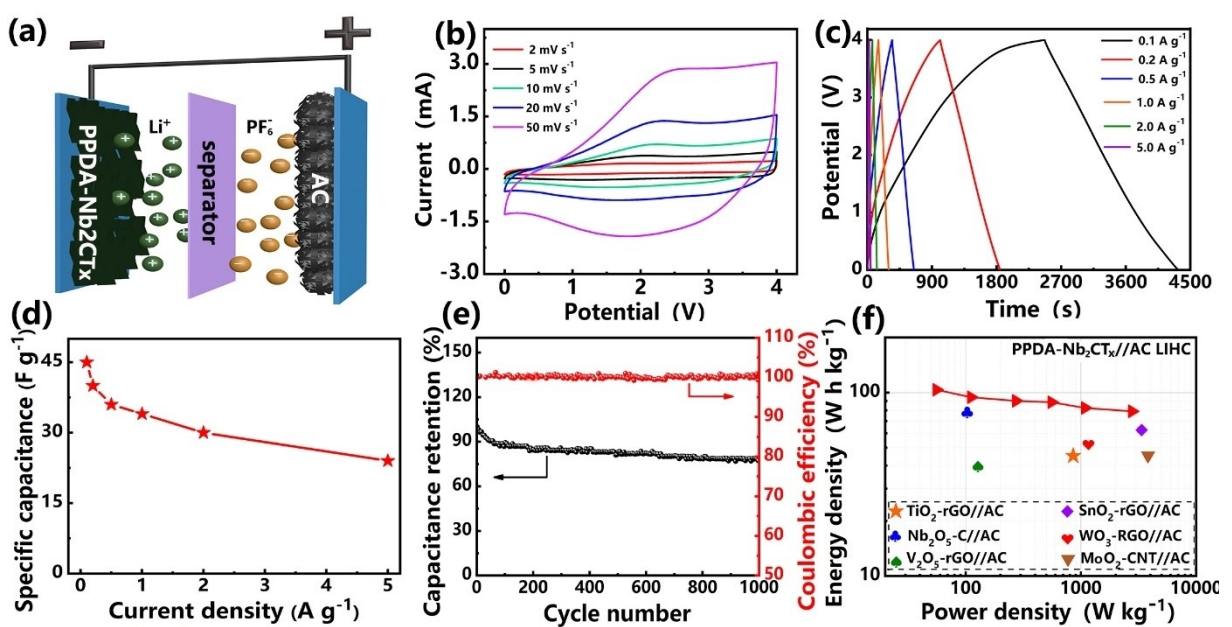


Figure 6. The electrochemical storage performance of PPDA-Nb<sub>2</sub>CT<sub>x</sub>//AC LIHC. a) Diagram of PPDA-Nb<sub>2</sub>CT<sub>x</sub>//AC LIHC. b) The CV curves at different scan rates. c) GCD curves at different current densities. d) Rate capability. e) Cyclic stability at 1.0 A g<sup>-1</sup>. f) Ragone plots of PPDA-Nb<sub>2</sub>CT<sub>x</sub>//AC and other LIHCs.

density of  $100.3 \text{ Wh kg}^{-1}$  at a power density of  $53.6 \text{ W kg}^{-1}$  and possesses  $2754.8 \text{ W kg}^{-1}$  at  $58.3 \text{ Wh kg}^{-1}$ . The method of electrostatic intercalation provides a guiding significance for developing the 2D materials with the enlarged interlayer spacing and the fast diffusion rate.

## Experimental Section

### Preparation of $\text{Nb}_2\text{CT}_x$ MXene

The  $\text{Nb}_2\text{CT}_x$  MXene was produced by etching Al from  $\text{Nb}_2\text{AlC}$  precursor (Carbon Technology Co., Ltd.) with HCl (AR, Nanjing Reagent) and LiF (99.0%, Alfa Aesar). Typically, 2.0 g LiF was dispersed in 40 mL 9 M HCl solution to form etching agent and 2.0 g  $\text{Nb}_2\text{AlC}$  was slowly added into above etching agent. The mixed solution was centrifuged and cleaned several times with deionized water (DI) until the pH closed to neutral after keeping stirred for 36 h at  $45^\circ\text{C}$ . Finally, the dark grey precipitation was collected and freeze-drying to obtain  $\text{Nb}_2\text{CT}_x$  MXene.

### Preparation of PPDA- $\text{Nb}_2\text{CT}_x$ powers

Firstly, 150 mg  $\text{Nb}_2\text{CT}_x$  powers were added in 50 mL DI water and an ultrasonic dispersion of 10 min was needed to prepare dispersion solution. Then, the above dispersion solution was dropped in 100 mL of 0.1 mg/mL PPDA ( $\geq 99.0\%$ , Aladdin) solution and kept stirring for 12 h under room temperature. Next, the mixed solution was placed for at least 6 hours and washed for three times by centrifugation at 5000 rpm. Ultimately, the composite powers were obtained by a freeze-drying (name as PPDA- $\text{Nb}_2\text{CT}_x$ ).

### Structural and electrochemical characterizations

The structural characterization, preparation of electrode, and assembly of LIBs and LIHCs, and electrochemical measurements can be found in the Supporting Information.

### Supporting Information

Additional references cited with the Supporting Information.<sup>[51–55]</sup>

### Acknowledgements

This work was supported by the National Natural Science Foundation of China (No. 52062030), the Found of the State Key Laboratory of Advance Processing and Recycling of Non-ferrous Metals, Lanzhou University of Technology (No. SKLAB02019008), Hongliu Youth Fund of Lanzhou University of Technology.

### Conflict of Interest

The authors declare no conflict of interest.

**Keywords:**  $\text{Nb}_2\text{CT}_x$  • enlarge interlayer spacing • diffusion dynamics • rate capability • lithium ions storage

- [1] S. Jeong, D. Yoo, J. T. Jang, M. Kim, J. Cheon, *J. Am. Chem. Soc.* **2012**, *134*, 18233–18236.
- [2] Q. Cui, Y. Zhong, L. Pan, H. Zhang, Y. Yang, D. Liu, F. Teng, Y. Bando, J. Yao, X. Wang, *Adv. Sci.* **2018**, *5*, 1700902.
- [3] F. Shahzad, M. Alhabeb, C. B. Hatter, B. Anasori, S. Man Hong, C. M. Koo, Y. Gogotsi, *Science* **2016**, *353*, 1137–1140.
- [4] Y. Liu, J. Wang, J. Wu, Z. Ding, P. Yao, S. Zhang, Y. Chen, *Adv. Energy Mater.* **2020**, *10*, 1903139.
- [5] K. Ji, J. Han, A. Hirata, T. Fujita, Y. Shen, S. Ning, P. Liu, H. Kashani, Y. Tian, Y. Ito, J.-i. Fujita, Y. Oyama, *Nat. Commun.* **2019**, *10*, 1–10.
- [6] W. Ren, H. Zhang, C. Guan, C. Cheng, *Adv. Funct. Mater.* **2017**, *27*, 1702116.
- [7] Q. Cui, Y. Zhong, L. Pan, H. Zhang, Y. Yang, D. Liu, F. Teng, Y. Bando, J. Yao, X. Wang, *Adv. Sci.* **2018**, *5*, 1700902.
- [8] F. Shahzad, M. Alhabeb, C. B. Hatter, B. Anasori, S. M. Hong, C. M. Koo, Y. Gogotsi, *Science* **2016**, *353*, 1137–1140.
- [9] M. Chhowalla, H. S. Shin, G. Eda, L. J. Li, H. Zhang, *Nat. Chem.* **2013**, *5*, 263–275.
- [10] X. Zhao, C. M. Hayner, M. C. Kung, H. H. Kung, *ACS Nano* **2011**, *5*, 8739–8749.
- [11] J. Xiao, D. Choi, L. Cosimescu, P. Koehl, J. Liu, J. P. Lemmon, *Chem. Mater.* **2010**, *22*, 4522–4524.
- [12] Y. Jing, Z. Zhou, C. R. Cabrera, Z. Chen, *J. Mater. Chem. A* **2014**, *2*, 12104–12122.
- [13] Y. Jing, Z. Zhou, C. R. Cabrera, Z. Chen, *J. Phys. Chem. C* **2015**, *117*, 25409–25413.
- [14] Q. Tang, Z. Zhou, *Prog. Mater. Sci.* **2013**, *58*, 1244–1315.
- [15] D. Magne, V. Mauchamp, S. Célérrier, P. Chartier, T. Cabioch, *Phys. Rev. B* **2015**, *91*, PhysRevB.91.201409.
- [16] O. Mashtalir, M. R. Lukatskaya, M. Q. Zhao, M. W. Barsoum, Y. Gogotsi, *Adv. Mater.* **2015**, *27*, 3501–3506.
- [17] B. Akuzum, E. Kumbar, K. Caglan, A. Narendra, P. Babak, *Energy Environ. Sci.* **2016**, *9*, 2847–2854.
- [18] X. Xie, M. Q. Zhao, B. Anasori, K. Maleski, C. E. Ren, J. Li, B. W. Byles, E. Pomerantseva, G. Wang, Y. Gogotsi, *Nano Energy* **2016**, *26*, 513–523.
- [19] H. W. Wang, M. Naguib, K. Page, D. J. Wesolowski, Y. Gogotsi, *Chem. Mater.* **2015**, *28*, 349–359.
- [20] M. Naguib, M. Kurtoglu, V. Presser, J. Lu, J. Niu, H. Min, L. Hultman, Y. Gogotsi, M. W. Barsoum, *Adv. Mater.* **2011**, *23*, 4248–4253.
- [21] W. Tian, A. Vahidmohammadi, Z. Wang, L. Ouyang, M. M. Hamed, *Nat. Commun.* **2019**, *10*, 2558.
- [22] C. Zhang, M. Naguib, M. Lukatskaya, Pual R. C. Kent, Y. Gogotsi, D. Jiang, *J. Phys. Chem. Lett.* **2018**, *9*, 1223–1228.
- [23] M. Naguib, V. Mochalin, M. W. Barsoum, Y. Gogotsi, *Adv. Mater.* **2014**, *26*, 992–1005.
- [24] J. Hu, B. Xu, C. Ouyang, Y. Zhang, S. A. Yang, *RSC Adv.* **2016**, *6*, 27467–27474.
- [25] M. Naguib, J. Halim, J. Lu, K. M. Cook, L. Hultman, Y. Gogotsi, M. W. Barsoum, *J. Am. Chem. Soc.* **2013**, *135*, 15966–15969.
- [26] O. Mashtalir, M. R. Lukatskaya, M.-Q. Zhao, M. W. Barsoum, Y. Gogotsi, *Adv. Mater.* **2015**, *27*, 3501–3505.
- [27] R. Liu, W. Cao, D. Han, Y. Mo, H. Zeng, H. Yang, W. Li, *J. Alloys Compd.* **2019**, *793*, 505–511.
- [28] J. Zhou, X. Zha, X. Zhou, F. Chen, G. Gao, S. Wang, C. Shen, T. Chen, C. Zhi, P. Eklund, *ACS Nano* **2017**, *11*, 3841–3850.
- [29] Q. Shan, X. Mu, M. Alhabeb, C. E. Shuck, D. Pang, X. Zhao, X. F. Chu, Y. Wei, F. Du, G. Chen, Y. Gogotsi, Y. Gao, Y. Dall' Agnese, *Electrochem. Commun.* **2018**, *96*, 103–107.
- [30] G. Wei, J. Li, Y. Ji, N. Klyui, V. Izotov, W. Han, *Chem. Eng. J.* **2017**, *317*, 1026–1036.
- [31] Z. Lin, P. Rozier, B. Dupoyer, P. L. Taberna, B. Anasori, Y. Gogotsi, P. Simon, *Electrochem. Commun.* **2016**, *72*, 50–53.
- [32] J. Luo, W. Zhang, H. Yuan, C. Jin, L. Zhang, *ACS Nano* **2016**, *11*, 2459–2469.
- [33] J. Luo, C. Fang, C. Jin, H. Yuan, O. Sheng, R. Fang, W. Zhang, H. Huang, Y. Gan, Y. Xia Chu, C. Liang, J. Zhang, W. Li, X. Tao, *J. Mater. Chem. A* **2018**, *6*, 7794–7806.
- [34] K. Ji, J. Han, A. Hirata, T. Fujita, Y. Shen, S. Ning, P. Liu, H. Kashani, Y. Tian, Y. Ito, J. Fujita, Y. Oyama, *Nat. Commun.* **2019**, *10*, 09742Z.
- [35] C. Tan, Z. Lai, H. Zhang, *Adv. Mater.* **2017**, *29*, 1701392.
- [36] H. Xi, D. P. Wang, X. H. Xiao, Y. X. Chen, H. B. Liu, Z. Q. Gu, *J. Nanosci. Nanotechnol.* **2019**, *19*, 7269–7277.
- [37] F. Wu, S. Zhao, J. Li, Y. Lu, Y. Su, L. Chen, L. Bao, J. Yao, X. Liu, *ACS Appl. Mater. Interfaces* **2019**, *11*, 12544–12553.

- [38] L. Du, H. Duan, Q. Xia, C. Jiang, Y. Yan, S. Wu, *ChemistrySelect* **2020**, *5*, 1186–1192.
- [39] M. Hu, R. Cheng, Z. Li, T. Hu, H. Zhang, C. Shi, J. Yang, C. Cui, C. Zhang, H. Wang, B. Fan, X. Wang, Y. Quan-Hong, *Nanoscale* **2019**, *12*, 763–771.
- [40] J. Xu, J. Zhang, W. Zhang, C.-S. Lee, *Adv. Energy Mater.* **2017**, *7*, 1700571.
- [41] V. Augustyn, Y. Gogotsi, *Joule* **2017**, *1*, 443–452.
- [42] J. Li, Q. Q. Yang, Y. X. Hu, M. C. Liu, Y. L. Chueh, *ACS Sustainable Chem. Eng.* **2019**, *2019*, 18357–18383.
- [43] Y. N. Ko, S. H. Choi, S. B. Park, Y. C. Kang, *Nanoscale* **2014**, *6*, 10511–10515.
- [44] Y. S. Zhang, B. M. Zhang, Y. X. Hu, J. Li, C. Lu, M. C. Liu, Y. L. Chueh, *Energy Storage Mater.* **2020**, *34*, 45–52.
- [45] H. K. Kim, D. Mhamane, M. S. Kim, H. K. Roh, V. Aravindan, S. Madhavi, K. C. Roh, K. B. Kim, *J. Power Sources* **2016**, *327*, 171–177.
- [46] L. Kong, C. Zhang, J. Wang, W. Qiao, L. Ling, D. Long, *ACS Nano* **2015**, *9*, 11200–11208.
- [47] Z. Chen, V. Augustyn, X. L. Jia, Q. e. Xiao, B. Dunn, Y. F. Lu, *ACS Nano* **2012**, *6*, 4319–4327.
- [48] M. Arnaiz, C. Botas, D. Carriazo, R. Mysyk, F. Mijanggos, T. Rojo, J. Ajuria, E. Goikolea, *Electrochim. Acta* **2018**, *284*, 542–550.
- [49] M. S. Kim, E. Lim, S. Kim, C. Jo, J. Chun, J. Lee, *Adv. Funct. Mater.* **2017**, *27*, 1603921.
- [50] S. Fleischmann, M. Zeiger, A. Quade, A. Knuth, V. Presser, *ACS Appl. Mater. Interfaces* **2018**, *10*, 18675–18684.
- [51] X. Dong, L. Chen, J. Liu, S. Haller, Y. Wang, Y. Xia, *Sci. Adv.* **2016**, *2*, 1501038.
- [52] P. Simon, Y. Gogotsi, B. Dunn, *Science* **2014**, *343*, 1210–1211.
- [53] V. Augustyn, P. Simon, B. Dunn, *Science* **2014**, *7*, 1597–1614.
- [54] L. Shen, H. Lv, S. Chen, P. Kopold, Y. Yan, *Adv. Mater.* **2017**, *29*, 1700142.
- [55] S. Wang, S. Liu, X. Li, C. Li, R. Zang, Z. Man, Y. Wu, P. Li, G. Wang, *Chem. Eur. J.* **2018**, *24*, 3873–3881.

Manuscript received: April 10, 2021

Revised manuscript received: May 22, 2021

Accepted manuscript online: May 30, 2021

Version of record online: June 10, 2021